RSC Advances

Highly active and stable nano NiO-MgO catalyst encapsulated by silica with core-shell structure for CO2 methanation

Journal:	*RSC Advances*
Manuscript ID:	RA-ART-11-2013-046569.R3
Article Type:	Paper
Date Submitted by the Author:	17-Mar-2014
Complete List of Authors:	Li, Yanrong; Lanzhou University, College of Chemistry and Chemical Engineering Lu, Gongxuan; Lanzhou Institute of Chemical Physics, Ma, Jiantai; College of Chemistry and Chemical Engineering, Lanzhou University,

Cite this: DOI: 10.1039/c0xx00000x

www.rsc.org/xxxxxx

ARTICLE TYPE

Highly active and stable nano NiO-MgO catalyst encapsulated by silica with core-shell structure for CO_2 methanation

Yanrong Li[a,b], Gongxuan Lu[*a,b], Jiantai Ma[a]

a College of Chemistry and Chemical Engineering, Lanzhou University, Lanzhou 730000, P.R .China

b State Key Laboratory for Oxo Synthesis and Selective Oxidation, Lanzhou Institute of Chemical Physics, Chinese Academy of Sciences, Lanzhou, 730000, P.R. China.

Received (in XXX, XXX) Xth XXXXXXXXX 20XX, Accepted Xth XXXXXXXXX 20XX

DOI: 10.1039/b000000x

ABSTRACT: The Ni-MgO nanoparticles (NPs) encapsulated by porous silica shell for CO_2 methanation were synthesized. The effects of Ni/Mg ratios in core-shell structured catalysts on CO_2 conversion and CH_4 selectivity were examined. Results showed that the NiO-MgO@SiO_2 catalyst with Ni/Mg ratio of 4/1 exhibited the highest catalytic activity (87% of conversion for CO_2 and 99% of selectivity for CH_4) and catalytic stability in the whole 100 h time on stream at low temperature (300 ◦C). It was found that the high catalytic activity and stability of this catalyst could be attributed to the isolated highly dispersed Ni NPs, which were obtained through the reduction of NiO-MgO solid solution protected by silica shell.

1. Introduction

It is well known that large scale fossil-fuel burning have resulted in a drastic carbon dioxide (CO_2) emission and the increasing of CO_2 concentration in atmospheric, which leads to the significant earth's climate change.[1] Hence, it is urgent in developing efficient CO_2 capture[2, 3] and utilization system to reduce its accumulation in the atmosphere. For example, membrane separation technologies have been introduced for carbon capture and storage (CCS) more recently.[4, 5]

As for the industrial scale usage and conversion of carbon dioxide, the transfer of CO_2 into chemicals have been intensively investigated,[6, 7] such as carbon dioxide reforming of methane (CH_4)[8, 9] and hydrogenation of carbon dioxide,[10, 11] because the products (synthesis gas, methane, methanol, dimethyl ether) of these reactions can be re-used as the industrial raw material or fuel directly. However, except for the reaction of methanation of carbon dioxide, other reactions need either relatively high temperature or high pressure to achieve the high yield of target products. By contrast, CH_4 can be obtained under mild conditions because CO_2 methanation is thermodynamically favourable and exothermic reaction.[12]

$$CO_2\,(g) + 4H_2\,(g) \rightarrow CH_4\,(g) + 2H_2O\,(l) \qquad (1)$$

$$\Delta H^0_{298K} = -164.9KJ\ /\ mol,\ \Delta G^0_{298K} = -133.5KJ\ /\ mol$$

Furthermore, CH_4 is one of the promising hydrogen carriers[13] considering existing infrastructure for transport and storage of natural gas.[14] Thus, methanation of carbon dioxide is the most advantageous catalytic process in CO_2 conversion. Nevertheless, the reduction of CO_2 to CH_4 is an 8 electrons process with significant kinetic limitation, which requires an active and cheaper catalyst to achieve acceptable rate and selectivity.

CO_2 methanation has been investigated using catalysts based on transition metals of VIIIB (Pd, Ru, Rh, Ni, and Co) supported on various metal oxides (SiO_2, Al_2O_3, ZrO_2, TiO_2, and CeO_2).[15-21] Although the noble metals (Pd, Rh and Ru) exhibit good activity, they are too expensive for large-scale industrial applications. Nickel is the most feasible catalytic component for CO_2 methanation due to its well-known high activity of hydrogenation and relatively low price compared to noble metal-based catalysts.[22-24]

For increasing catalytic activity, it is important to get the active component highly dispersed. Thus, designing catalysts with well-dispersed nanostructured metallic Ni particles is necessary. In order to improve the dispersion of active component, MgO is widely selected as a support due to its low cost, stability and strong Lewis basicity for strong adsorption for CO_2.[25, 26] It has been reported that the catalysts modified with MgO showed much higher selectivity for CH_4 and higher CO_2 and H_2 conversions on CO_2 methanation in comparison with traditionally Pd-based or Ni-based catalysts.[18, 27] Moreover, formation of NiO-MgO solid solution can be easy achieved from mixture of NiO and MgO during calcination.[28] This solid solution can be used as sources of small Ni^0 particles.[29, 30]

A challenge of preparing these nanostructured catalysts is how to prevent unstable and active metallic NPs from rapidly sintering during the exothermic methanation reaction which may leads to catalyst deactivation.[29] In order to reach this goal, encapsulation of metallic NPs with a porous shell such as silica or alumina were

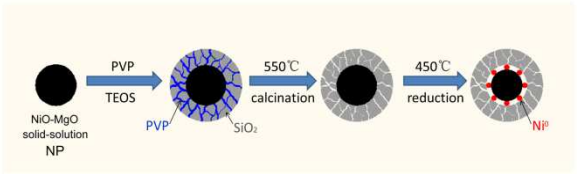

Scheme 1 preparation process of Ni-MgO@SiO_2 catalyst

explored.[30] It was reported that metal NPs isolated by a porous silica shell were thermally stable and against sintering at high temperatures.[31-33] There were two ways to prepare silica shell. One is reverse micelle technique,[34] another is modified Stöber method.[35, 36]

In this paper, NiO, MgO and NiO-MgO NPs which were prepared via surfactant assisted chemical co-precipitation and followed thermal treatment were encapsulated by porous silica shell by modified Stöber method. The characteristics of NiO-MgO@SiO_2 were tuned by changing the Ni/Mg ratio, and the CO_2 methanation performances of NiO-MgO@SiO_2 were investigated. Based on carefully comparison results with various Ni/Mg ratios, NiO-MgO@SiO_2 catalyst with Ni/Mg ratio of 4/1 exhibited excellent catalytic performance for CO_2 methanation at 300 ◦C.

2. Experimental

2.1 Catalyst preparation

2.1.1 Preparation of metal oxide NPs

All chemicals (AR grade) were employed without further purifications.

The oxide NPs with Ni/Mg ratio of 4/1 were prepared by surfactant assisted chemical co-precipitation method. Typically, 2.321 g of $Ni(NO_3)_2{\cdot}6H_2O$ (Shanghai No.2 Reagent Factory, China) and 0.512g of $Mg(NO_3)_2{\cdot}6H_2O$ (Shanghai Reagent Factory, China) were dissolved in 40 mL of deionized water. The solution was then added dropwise into a solution that contained 100 mL of deionized water, 0.330 mg of polyethylene glycol (PEG, MW= 20,000, Shanghai Reagents Factory, China) and 1.0 g NaOH. The resulting solution was stirred for 1 h at room temperature. The precipitate was collected by centrifugation and washed several times with deionized water and ethanol. The obtained solid was dried at 60 ◦C for 24 h and then calcined in static air at 400 ◦C for 2 h. Samples with different Ni/Mg mole ratios (1/0, 5/1, 3/1, 1/1, 1/3, and 0/1) were also prepared by a similar process. The oxides were labeled as Ni_xMg_yO (x+y=1), where x/y stood for the Ni/Mg mole ratio in the parent solution.

2.1.2 Metal oxides NPs encapsulated by porous silica

The core-shell structured $Ni_xMg_yO@SiO_2$ samples were synthesized *via* a modified Stöber method.[36] Certain amount of oxide NPs (for example, $Ni_{0.8}Mg_{0.2}O$ NPs of 0.2 g) was first dispersed in a mixture of ethanol (100 mL) and poly-(vinylpyrrolidone) (PVP, K30, 1.0 g average Mr = 10,000, Shanghai Reagents Factory, China). After the solution was stirred for 12 h, 10 mL $NH_3{\cdot}H_2O$ (25 wt. %) was added. The mixed suspension was homogenized for 0.5 h by ultrasonication. Then an ethanol solution (20 mL) of tetraethoxysilane (TEOS, ≥99%, 0.1 mL) was injected into the suspension very slowly. Two hours later, the products were collected by centrifugation, washed with distilled water and ethanol for several times. The obtained solid was dried at 60 ◦C for 6 h then calcined at 550 ◦C for 2 h in static air to remove the PVP. The as-calcined samples were denoted as NiO@SiO_2, $Ni_{0.83}Mg_{0.17}O@SiO_2$, $Ni_{0.8}Mg_{0.2}O@SiO_2$, $Ni_{0.75}Mg_{0.25}O@SiO_2$, $Ni_{0.5}Mg_{0.5}O@SiO_2$, $Ni_{0.25}Mg_{0.75}O@SiO_2$ and MgO@SiO_2, respectively. All the as-calcined $Ni_xMg_yO@SiO_2$ samples were in situ reduced in a 50 vol % H_2/N_2 mixture (flow rate 60 mL min^{-1}) at 500 ◦C for 2 h, and the obtained catalysts were denoted as Ni@SiO_2 and $Ni_xMg_yO@SiO_2$-R (y＞0), respectively.

Standard catalyst NiO(60%)/SiO_2 with a Ni loading of 60 wt% was prepared by the conventional impregnation method. SiO_2 (438 m^2 g^{-1}, 0.99 cm^{-3} g^{-1}, 30-45 mesh) 2.0 g was added to $Ni(NO_3)_2{\cdot}6H_2O$ solution (25.197 g, 40mL). The resulting mixture was stirring for 18 h and then dried at 110 ◦C for 4 h, followed by calcination in air at 400 ◦C for 2 h. The obtained sample was denoted as NiO(60%)/SiO_2-IMP. After in situ reduction the obtained catalysts were denoted as Ni(60%)/SiO_2-IMP.

2.2 Catalyst Characterization

The Ni and Mg contents in the $Ni_xMg_yO@SiO_2$ catalysts were determined by atomic absorption spectroscopy.

XRD patterns were recorded on Rigaku B/Max-RB X-ray diffractometer with a nickel filtrated Cu Kα radiation (0.15046 nm) from 15 to 85°. Crystallite sizes of nanoparticles were calculated using Scherrer equation:

$$D_{(h\,k\,l)} = \frac{K\lambda}{\beta\cos\theta} \qquad (2)$$

where K is the shape factor (0.89) of the average crystalline, λ is the wavelength (0.154 nm), β is the width of the peak at half height, and θ is Bragg angle. X-ray photoelectron spectroscope (XPS) analyses of the catalysts were performed using VG Scientific ESCALAB250-XPS photoelectron spectrometer with Mg Kα X-ray resource. The binding energy (BE) was calibrated by the C_{1s} binding energy of 284.6 eV. TEM (transmission electron microscopy) images and energy-dispersed X-ray spectroscopy (EDX) measurements were performed on the FEI F20 (Netherlands) high-resolution transmission electron microscopy under a working voltage of 200 kV. Samples for TEM analyses were sonicated in ethanol and then transferred as suspension to carbon-coated copper grids. The nitrogen adsorption and desorption isotherms at -196 °C were recorded on a Micromeritics ASAP 2020 apparatus. Prior to the tests, catalysts were degassed at 150 ◦C for 5 h. H_2 temperature-programmed reduction measurements (H_2-TPR) were carried out in a vertical quartz reactor equipped with a thermal conductivity detector (TCD). Prior to the H_2-TPR measurements, catalysts (25 mg) were pretreated at 300 ◦C for 0.5 h in flowing N_2 (40 mL min^{-1}) to remove any moisture and adsorbed impurities. After cooling the reactor to the room temperature, the catalysts were heated at a rate of 10 ◦C min^{-1} from 50 to 700 ◦C in a flow of 5 vol % H_2/Ar reducing mixture (35 mL min^{-1}). The hydrogen consumption was measured by a TCD detector. Thermogravimetric/differential scanning calorimeter (TG-DSC) measurements were conducted using NETZSCH STA 449F3 thermogravimetric analyzer from room temperature to 600 ◦C with a heating rate of 10 ◦C min^{-1} under atmosphere. H_2-Chemisorption was performed by using pulse technique in a U-shaped quartz tube on a Micromeritics ChemiSorb 2750 Instrument (Micromeritics, USA) with a thermal conductivity detector (TCD). The Ni dispersion of the catalysts calculated based on the following equation:

$$D\,(\%) = \frac{2 \times S_f \times M \times V_{ad}}{m \times W \times V_m \times d_r} \times 100 \qquad (3)$$

Where: S_f = stoichiometry factor (the Ni/H molar ratio in the chemisorption) =1; M= the molecular weight of Ni (58.69g mol^{-1}); V_{ad} = the volume of chemisorbed H_2 at standard temperature and pressure conditions (mL g^{-1}); m= the weight of sample (g); W=the weight fraction of Ni in the sample as determined by AAS; V_m = molar volume of H_2 (22414 mL mol^{-1}) at STP; dr = the reduction degree of Ni.

2.3 Catalytic activity measurement

The methanation of CO_2 reaction was conducted in a quartz fix-bed down-flow reactor (i.d. 6mm) at atmospheric pressure. Before catalytic tests, each catalyst (50 mg) was in situ reduced then purged in N_2 and cooled to room temperature. Then CO_2 methanation reactions were carried out with a total mixture flow of 90 mL min^{-1} ($H_2/CO_2/N_2$=4:1:4, v/v/v, N_2 is the internal reference,) in the temperature range from 200 to 500 ◦C with the increment of 50 °C and stayed at each temperature stage for 60 min. The composition of effluent gas was analyzed by two on-line chromatographs equipped with TCD. An ice bath was set up between the reactor exit and the sampling port in order to remove water from the effluent gas used for GC analysis. An off-line flame ionization detector (FID) was used for analyzing produced hydrocarbons byproducts. Catalysts performances were analysed by measuring CO_2 conversion (X_{CO2}) and CH_4 selectivity (S_{CH4}), which were calculated by applying the following equations:

$$X_{CO_2}(\%) = \frac{F_{CH_4 out} + F_{COout}}{F_{CH_4 out} + F_{COout} + F_{CO_2 out}} \times 100 \quad (4)$$

$$S_{CH_4}(\%) = \frac{F_{CH_4 out}}{F_{CH_4 out} + F_{COout}} \times 100 \quad (5)$$

3. Results and discussion

3.1 Catalyst characterization

The TG and DSC curves of $Ni(OH)_2$, $Mg(OH)_2$, and $Ni_{0.8}Mg_{0.2}(OH)_2$ (representing the $Ni_xMg_y(OH)_2$) were shown in Fig.1. The TG curve showed that the weight loss of hydroxides were approximately 19%, 31% and 20% for $Ni(OH)_2$, $Mg(OH)_2$ and $Ni_{0.8}Mg_{0.2}(OH)_2$, respectively. It can be seen that $Ni(OH)_2$, $Mg(OH)_2$ and $Ni_{0.8}Mg_{0.2}(OH)_2$ showed endothermic peak at

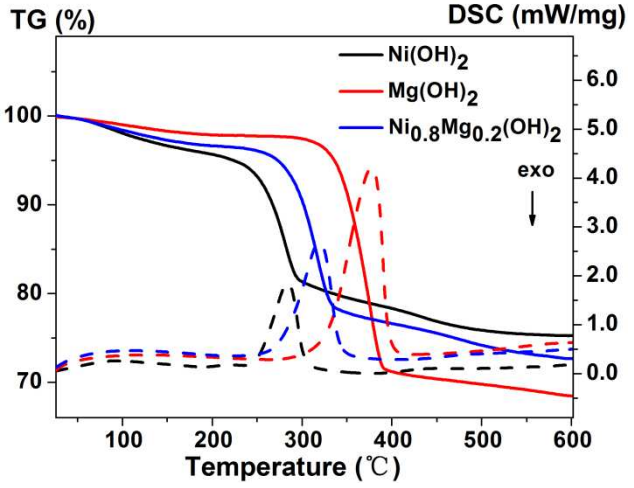

Fig. 1 TG and DSC curves of $Ni(OH)_2$, $Mg(OH)_2$, and $Ni_{0.8}Mg_{0.2}(OH)_2$

284 ◦C, 377 ◦C and 318 ◦C, respectively. $Ni_{0.8}Mg_{0.2}(OH)_2$ showed a characteristic endothermic peak at 318 ◦C differing from that of either $Ni(OH)_2$ or $Mg(OH)_2$, indicating that $Ni_{0.8}Mg_{0.2}(OH)_2$ is a new single phase but not a physical mixture of $Ni(OH)_2$ and $Mg(OH)_2$.

The XRD patterns of $Ni_xMg_yO@SiO_2$ with different Ni/Mg ratios after calcination at 550 ◦C were displayed in Fig. 2A. Fig. 2A showed peaks attributed to the presence of cubic NiO and MgO in sample $NiO@SiO_2$ and $MgO@SiO_2$, respectively. Since both NiO and MgO have the same crystal structure of sodium chloride type, the NiO-MgO solid solution can be formed during calcination. The peaks located at 37.2°, 43.2°, 62.7°, 75.2° and 79.2° in the $Ni_{0.83}Mg_{0.17}O@SiO_2$, $Ni_{0.8}Mg_{0.2}O@SiO_2$, $Ni_{0.75}Mg_{0.25}O@SiO_2$, $Ni_{0.5}Mg_{0.5}O@SiO_2$ and $Ni_{0.25}Mg_{0.75}O@SiO_2$ patterns were attributed to the formation of a NiO-MgO solid solution.

Although the positions of the characteristic XRD peaks of NiO and MgO were very close, the formation of solid solution was supported by the fact that the peaks of NiO-MgO (62-63°) were shifted from MgO to NiO with increasing Ni content (Fig. 2B) as shown in Reference.[37] It can also be evidenced that there were no Ni_2SiO_4 and Mg_2SiO_4 species detected by XRD characterization

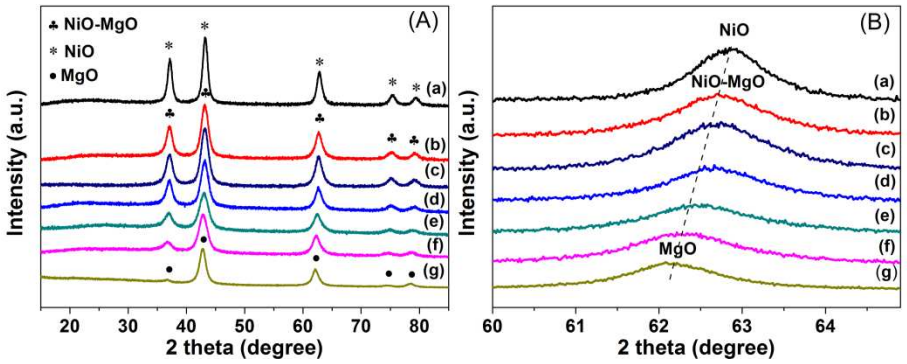

Fig. 2 (A) superposition XRD patterns and (B) enlargement of patterns in Bragg angle range 61-64° of the NiO-MgO@SiO_2 catalysts calcined at 550 °C with different Ni/Mg ratios, (a):$NiO@SiO_2$, (b):$Ni_{0.83}Mg_{0.17}O@SiO_2$, (c):$Ni_{0.8}Mg_{0.2}O@SiO_2$, (d):$Ni_{0.75}Mg_{0.25}O@SiO_2$, (e):$Ni_{0.5}Mg_{0.5}O@SiO_2$, (f):$Ni_{0.25}Mg_{0.75}O@SiO_2$, (g):$MgO@SiO_2$.

Table 1 Characteristics of the core-shell Catalysts before reduction

Catalysts	Actual amount (%)		S_{BET} ($m^2 g^{-1}$)	Pore volume ($cm^3 g^{-1}$)	Average pore diameter (nm)	D metal oxide (nm)	
	Ni	Mg				36.9°	43°
$NiO@SiO_2$	65.2	/	115.2	0.394	11.563	12.0	10.8
$Ni_{0.83}Mg_{0.17}O@SiO_2$	62.1	5.0	109.2	0.252	9.232	10.2	9.6
$Ni_{0.8}Mg_{0.2}O@SiO_2$	59.4	6.3	134.3	0.554	15.458	9.9	9.0
$Ni_{0.75}Mg_{0.25}O@SiO_2$	56.8	7.7	128.7	0.276	8.641	10.8	9.7
$Ni_{0.5}Mg_{0.5}O@SiO_2$	47.1	16.5	163.4	0.419	10.265	10.5	9.1
$Ni_{0.25}Mg_{0.75}O@SiO_2$	26.5	34.2	148. 6	0.347	9.334	9.3	9.1

in all samples (Fig. 2A), suggesting the absence of interaction between NiO-MgO cores and silica shell in our case. Furthermore, with an increase in Mg content, the diffraction patterns showed much broader and less intense peaks, indicating decreased crystallinity and particle size of cores. The crystallite size and the BET areas of fresh $Ni_xMg_yO@SiO_2$ catalysts with different Ni/Mg ratios were listed in Table 1.

The morphology of the catalysts was studied by the transmission electron microscopy. Fig. 3A and B showed the TEM images of $Ni_{0.8}Mg_{0.2}O@SiO_2$ catalyst before reduction. It was observed that core $Ni_{0.8}Mg_{0.2}O$ NPs were coated with silica shell and well-dispersed. Fig. 3C showed the distribution of core $Ni_{0.8}Mg_{0.2}O$ NPs size of $Ni_{0.8}Mg_{0.2}O@SiO_2$ catalyst determined by 100 particles from Fig. 3A. Average size of $Ni_{0.8}Mg_{0.2}O$ NPs (about 6nm in diameter) was smaller than that calculated from the XRD data (Table 1). The particles were identified as containing Ni, Mg, and Si by EDX analysis in Fig. 3D.

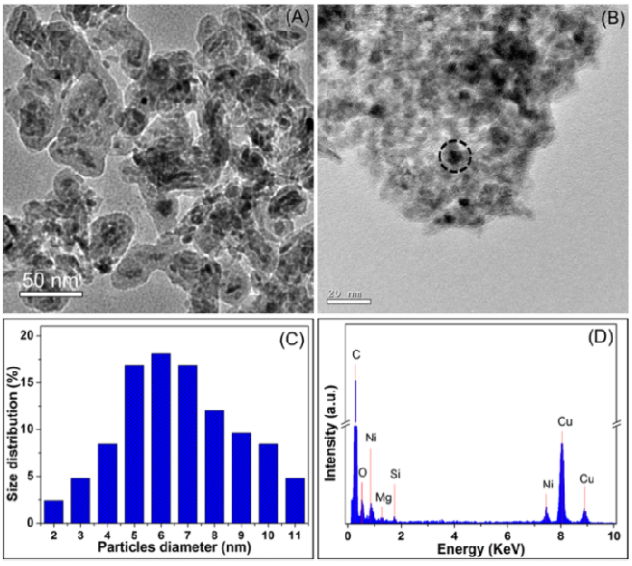

Fig. 3 (A) Low magnification, and (B) high magnification TEM images of $Ni_{0.8}Mg_{0.2}O@SiO_2$ catalyst before reduction; (C) core $Ni_{0.8}Mg_{0.2}O$ NPs size distribution determined from 100 particles obtained from (A); (D) $Ni_{0.8}Mg_{0.2}O@SiO_2$ catalyst before reduction with EDX analysis of the circled area in (B).

Table S1 (ESI.†) provided the binding energy of the surface elements of the catalysts $Ni_xMg_yO@SiO_2$ with Ni/Mg ratios from 5/1 to 1/3 measured by XPS. According to the binding energy data, the valence of the surface elements were Ni^{2+}, Mg^{2+}, Si^{4+} and O^{2-}, respectively. In Table S1 there was a progressive B.E. shift of the Ni2p peak, about 0.9 eV shift from $Ni_{0.83}Mg_{0.17}O@SiO_2$ to $Ni_{0.25}Mg_{0.75}O@SiO_2$ catalysts, whereas the binding energy of Ni 2p of NiO was 853.7 eV. This shift of binding energy indicated a strong interaction between NiO and MgO, suggesting the formation of NiO-MgO solid solution.[38, 39]

X-ray photoelectron spectra of Ni 2p in fresh $Ni_xMg_yO@SiO_2$ catalyst with Ni/Mg ratios from 5/1 to 1/3 were shown in Fig.4. It can be seen that Ni $2p_{3/2}$ photoelectron spectra of $Ni_{0.83}Mg_{0.17}O@SiO_2$ catalyst exhibited a shoulder characteristic of the NiO (B.E. 1.7 eV higher than that of the Ni $2p_{3/2}$ main peak). However, there was a progressive change in the shape of the Ni $2p_{3/2}$ with a considerable blunting from the $Ni_{0.83}Mg_{0.17}O@SiO_2$ catalyst to the $Ni_{0.25}Mg_{0.75}O@SiO_2$ catalyst. Meanwhile, the shoulder peak did not disappear until the Ni/Mg ratio became 1/1. It was reported that the Ni 2p photoelectron

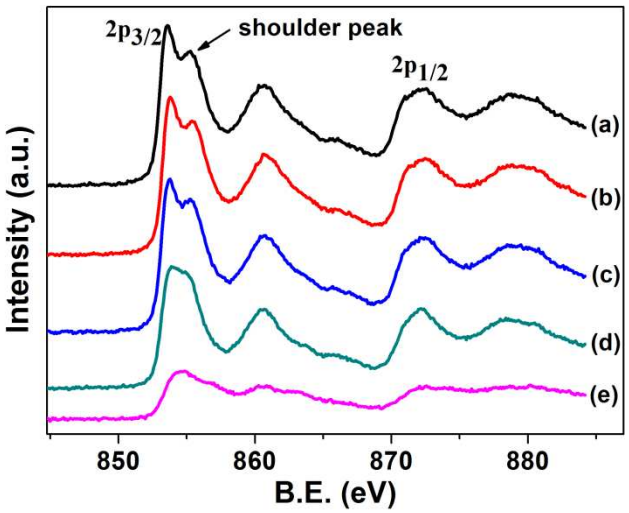

Fig. 4 XPS spectra of the catalysts calcined at 550°C with different Ni/Mg ratios, (a): $Ni_{0.83}Mg_{0.17}O@SiO_2$ (b): $Ni_{0.8}Mg_{0.2}O@SiO_2$ (c): $Ni_{0.75}Mg_{0.25}O@SiO_2$ (d): $Ni_{0.5}Mg_{0.5}O@SiO_2$ (e): $Ni_{0.25}Mg_{0.75}O@SiO_2$

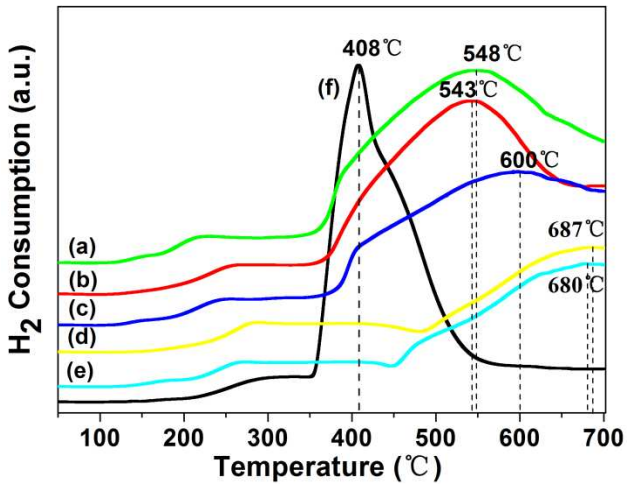

Fig. 5 H_2-TPR profile of as-calcined catalysts with different Ni/Mg ratios (a): $Ni_{0.8}Mg_{0.2}O@SiO_2$ (b): $Ni_{0.83}Mg_{0.17}O@SiO_2$ (c): $Ni_{0.75}Mg_{0.25}O@SiO_2$ (d): $Ni_{0.25}Mg_{0.75}O@SiO_2$ (e): $Ni_{0.5}Mg_{0.5}O@SiO_2$ (f): $NiO@SiO_2$.

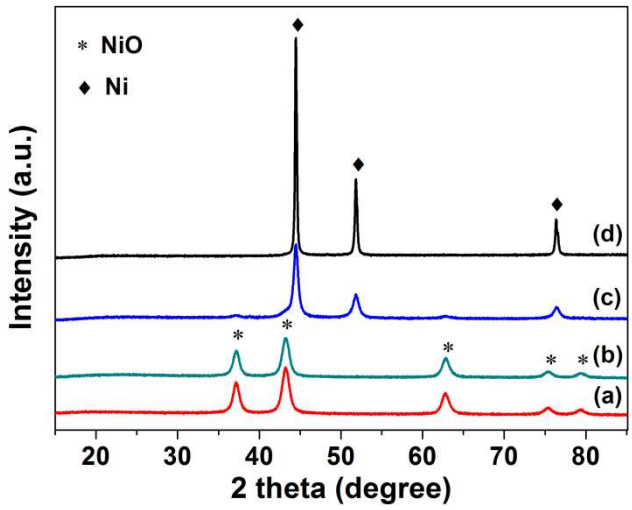

Fig. 6 XRD patterns of NiO catalysts (a) before and (d) after reduction and $NiO@SiO_2$ catalysts (b) before and (c) after reduction.

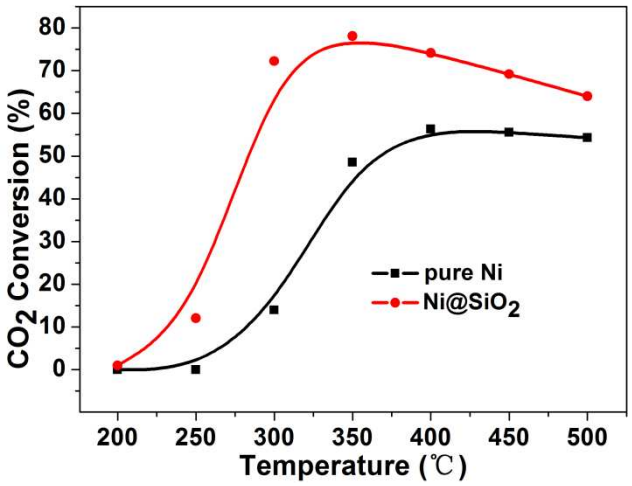

Fig. 7 CO_2 conversion versus temperature on pure Ni and $Ni@SiO_2$

spectra of $Ni_xMg_{(1-x)}O(x<0.5)$ solid solution did not exhibit the shoulder peak.[40, 41] Thus we can conclude that it was preferential to form a surface "NiO rich" solid solution when Ni/Mg was greater than 1/1 at the same calcination temperature. But when Ni/Mg was smaller than 1/1, NiO would diffuse from the outermost layer into a deeper layer to form a more stable surface "MgO rich" solid solution.[42] For catalytic reaction, surface "NiO rich" solid solution was more useful as it was easier to form Ni^0 active centers from surface "NiO rich" solid solution than that from surface "MgO rich" solid solution during the pre-reduction process.

The H_2-TPR profiles of as-calcined $Ni_xMg_yO@SiO_2$ catalysts with different Ni/Mg ratios were shown in Fig. 5. For $NiO@SiO_2$, the major peak centered at 408 ◦C was corresponded to the reduction of free-NiO. The shape of its peak and the maximum value was very similar to that of pure NiO NPs which was used as core material. By comparison of catalysts with different Ni/Mg ratios, we found that the reduction peaks shifted to higher values and broadened with the addition of MgO in the catalysts. It indicated the interaction between MgO and NiO probably hindered the reduction of NiO, owing to the formation of a NiO-MgO solid solution.[43] Zecchina et al. reported that the NiO-MgO solid solutions were reduced by H_2 in two different ways: in the temperature range 398-820 ◦C, mainly the Ni^{2+} ions located on the surface were reduced, while the Ni^{2+} located in the bulk could be reduced at temperature higher than 820 ◦C.[44] Therefore, metal Ni NPs were generated from Ni^{2+} ions located on the surface of solid solution in our catalysts. Nevertheless, the reducibility of NiO decreased as the Ni loading was lowered, which might due to lower Ni loading decreasing the fraction of 'easy-reducible' NiO.[28]

3.2 Catalytic performance

3.2.1 The effect of the silica shell

Fig.6 showed the XRD data of NiO and $NiO@SiO_2$ before and after reduction, respectively. It was observed that the patterns of NiO and $NiO@SiO_2$ before reduction have the similar peaks. According to Scherrer equation, the average D value (D is the crystallite size) of the NiO particles in NiO and $NiO@SiO_2$ samples were 10.6 nm and 10.8 nm, respectively, indicating that the size of NiO NPs did not change before and after encapsulating by silica shell. The characteristic diffraction peaks of the Ni (JCPDS Card No. 87-0712) were detected in the reduced NiO and $NiO@SiO_2$ samples. Compared with the reduced $NiO@SiO_2$, characteristic diffraction peaks of Ni in the reduced NiO sample exhibited stronger and narrowed Ni metal diffraction peaks, indicating that the Ni particles suffered from sintering during reduction. According to Scherrer equation, the average D_{111} of the Ni particles in reduced NiO and $NiO@SiO_2$ samples were 36.2 nm and 15.3 nm, respectively. It was confirmed that the silica shell could protect the Ni from aggregating during the reduction process at high temperature. The comparison of catalytic activities between pure Ni and $Ni@SiO_2$ were carried out to further prove that sintered Ni without SiO_2 protection gave the lower catalytic activities than $Ni@SiO_2$.

Fig. 7 showed the catalytic activities of the pure Ni and $Ni@SiO_2$ for CO_2 methanation. The pure Ni catalyst and $Ni@SiO_2$ reduced from NiO and $NiO@SiO_2$ samples, respectively. Pure Ni showed lower CO_2 conversion than $Ni@SiO_2$ at all temperature range, and no CO_2 conversion below

250 ◦C. It reached the maximum CO_2 conversion (56 %) and CH_4 selectivity (80 %) at 400 ◦C (in Fig.S1, ESI†). By contrast, the sample Ni@SiO_2 exhibited significantly improved CO_2 conversion (78 %) and CH_4 selectivity (98 % in Fig.S1) at 350 ℃. It was confirmed that the confinement effect of silica shell contributed to controlling the size of the Ni NPs which could affect the activity of CO_2 methanation.

3.2.2 The effect of the magnesium modifier

The activity of the catalysts with different Ni/Mg ratios for CO_2 methanation were monitored by means of the conversion of CO_2 and the selectivity for CH_4 from 200 ◦C to 500 ◦C as shown in Fig. 8A and 8B. It was found that CO_2 conversion of the Ni_xMg_yO@SiO_2-R catalysts increased with the enhancement of Ni/Mg ratios from 0/1 to 4/1, and decreased with the further increasing the Ni/Mg ratios from 4/1 to 5/1. The Ni_xMg_yO@SiO_2-R catalyst with the Ni/Mg ratios of 5/1, 4/1 and 3/1 exhibited a dramatically enhanced low-temperature activity. The MgO@SiO_2-R showed the lowest activity, with a CO_2 conversion and CH_4 selectivity (Fig. 8B) of only 42% and 27% at 500 ◦ C, respectively. This indicated that the catalyst $Ni_{0.25}Mg_{0.75}O$@SiO_2 was unable to provide sufficient Ni active sites for the reaction as suggested by results in Fig. 5. (There was not enough Ni active sites can be reduced from surface "MgO rich" solid solution.) Particularly, $Ni_{0.8}Mg_{0.2}O$@SiO_2-R possessed the highest CO_2 conversion (87%) at 300 ◦C, and showed high CH_4 selectivity of 99% below 400 ◦C In Fig. 8B, all the catalysts with the Ni/Mg ratio above 1/1 showed high selectivity to CH_4 (99%) in the studied temperature range. However, the selectivity of CH_4 suffered from a significant decline and the selectivity of CO increased with the further increase of Mg content in the catalyst. It indicated that over addition of MgO will reduce the Ni active center on the surface of catalyst, leading to the conversion of CO_2 to CO instead of CH_4.

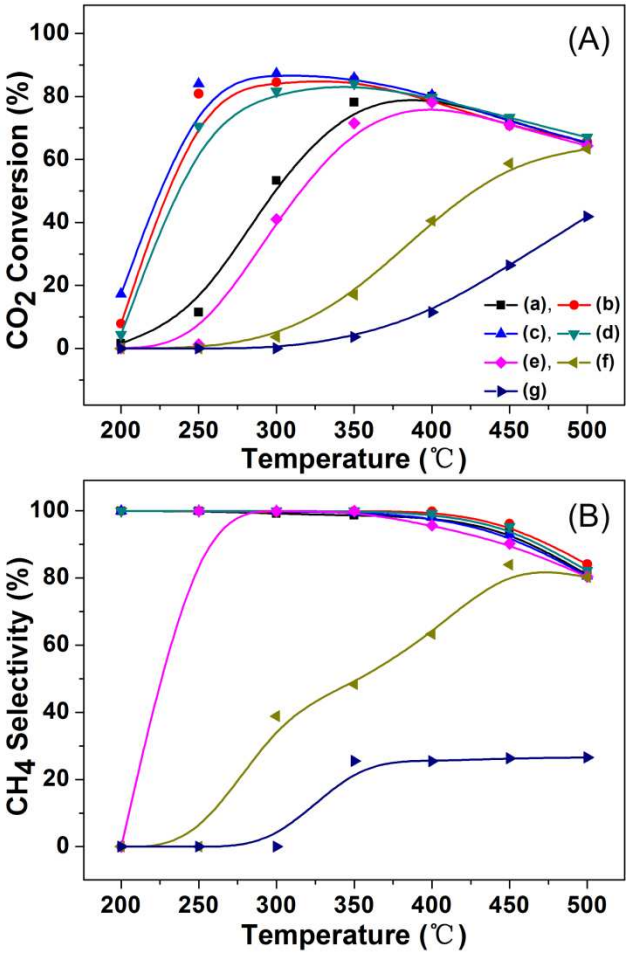

Fig. 8 The curves of (A) CO_2 conversion, (B) CH_4 selectivity versus temperature on catalysts (a): Ni@SiO_2 catalyst (b): $Ni_{0.83}Mg_{0.17}O$@SiO_2-R (c): $Ni_{0.8}Mg_{0.2}O$@SiO_2-R (d): $Ni_{0.75}Mg_{0.25}O$@SiO_2-R (e): $Ni_{0.5}Mg_{0.5}O$@SiO_2-R (f): $Ni_{0.25}Mg_{0.75}O$@SiO_2-R (g): MgO@SiO_2-R

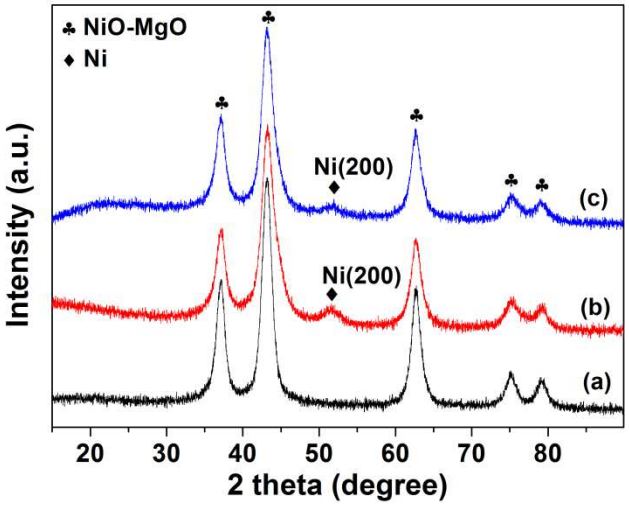

Fig.9 XRD patterns of $Ni_{0.8}Mg_{0.2}O$@SiO_2 catalysts (a) after calcination at 550 °, (b) after reduction and (c): after 8 h reaction

To further demonstrate that the catalytic activity was improved with high Ni dispersion which was caused by addition of MgO, the XRD measures of $Ni_{0.8}Mg_{0.2}O$@SiO_2 catalyst after calcination, reduction, and 8h reaction were conducted and their patterns were displayed in Fig. 9. In the pattern of $Ni_{0.8}Mg_{0.2}O$@SiO_2-R sample after reduction, it can be seen that the NiO from the NiO-MgO was reduced to Ni^0 (51.7°) after H_2 pretreatment. The diffraction peak of Ni^0 (44.5°) was hard to be distinguished from the peak of the NiO-MgO (43.2°) owing to its overlapping with each other. The diffraction peak of metallic Ni (51.7°) was very weak and broadening, indicating that Ni NPs were well dispersed and small. There were researches reported that the formation of NiO-MgO solid solution could make the reduction of NiO in NiO-MgO solid solution much more difficult than that of pure NiO, leading to the formation of small nickel NPs on the surface.[25, 29] Therefore, the Ni NPs reduced from $Ni_{0.8}Mg_{0.2}O$@SiO_2 were small in the solid solution. However, the crystallite size of metallic Ni can't be calculated using Scherrer equation owing to the diffraction peak broadening. Meanwhile, comparing with the $Ni_{0.8}Mg_{0.2}O$@SiO_2-R, there was no remarkable change in the diffraction pattern of $Ni_{0.8}Mg_{0.2}O$@SiO_2-8h, suggesting that the Ni NPs were not sintered after methanation reaction for 8 h. Thus, the $Ni_{0.8}Mg_{0.2}O$ solid solution enabled the catalyst to form small size Ni particles and improved the dispersion of the Ni active sites. Small and well dispersed Ni^0 particles protected by silica shell made the $Ni_{0.8}Mg_{0.2}O$@SiO_2 catalyst exhibit better activity on CO_2

menthanation.

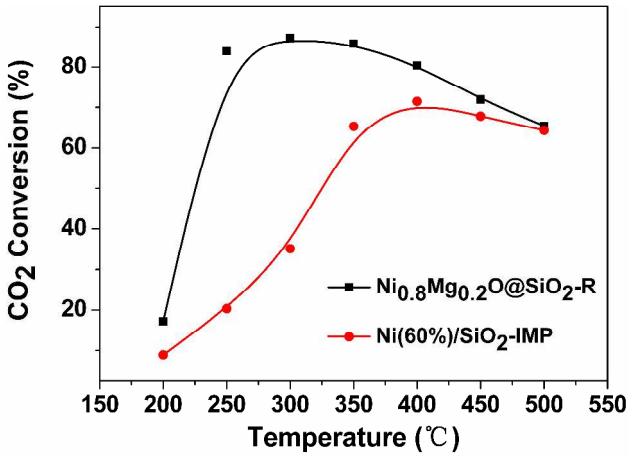

Fig. 10 CO_2 conversion versus temperature on $Ni_{0.8}Mg_{0.2}$@SiO_2-R and Ni(60%)/SiO_2-IMP. Reaction condition: H_2/CO_2=4, GHSV=60,000 mL (g h)$^{-1}$, 1 atm

The NiO(60%)/SiO_2-IMP catalyst was studied as the standard catalyst. Fig. 10 showed the CO_2 conversion versus temperature on $Ni_{0.8}Mg_{0.2}$@SiO_2-R and Ni(60%)/SiO_2-IMP. The temperature at which Ni(60%)/SiO_2-IMP catalyst exhibited the maximum CO_2 conversion (70%) was 100 ◦C higher than that of $Ni_{0.8}Mg_{0.2}O$@SiO_2-R catalyst. Ni(60%)/SiO_2-IMP catalyst gave relative low CO_2 conversion (35%) at 300 ℃, whereas $Ni_{0.8}Mg_{0.2}O$@SiO_2-R catalyst gave CO_2 conversion of 87% at same temperature. Compared with the Ni(60%)/SiO_2-IMP catalyst, the $Ni_{0.8}Mg_{0.2}O$@SiO_2-R showed significantly improved CO_2 conversion at low temperature. Meanwhile, $Ni_{0.8}Mg_{0.2}O$@SiO_2-R showed higher CH_4 selectivity than Ni(60%)/SiO_2-IMP at the whole temperature range (in Fig.S2, ESI†). H_2-Chemisorption was performed to characterize the Ni dispersion of the catalyst. The dispersion of Ni over $Ni_{0.8}Mg_{0.2}O$@SiO_2-R and Ni(60%)/SiO_2-IMP catalyst calculated using equation (3) were 19.8 and 4.7%, respectively. It can be concluded that $Ni_{0.8}Mg_{0.2}O$@SiO_2-R catalyst with higher Ni dispersion enhanced low-temperature CO_2 conversion and CH_4 selectivity in comparison with Ni(60%)/SiO_2-IMP with lower Ni dispersion.

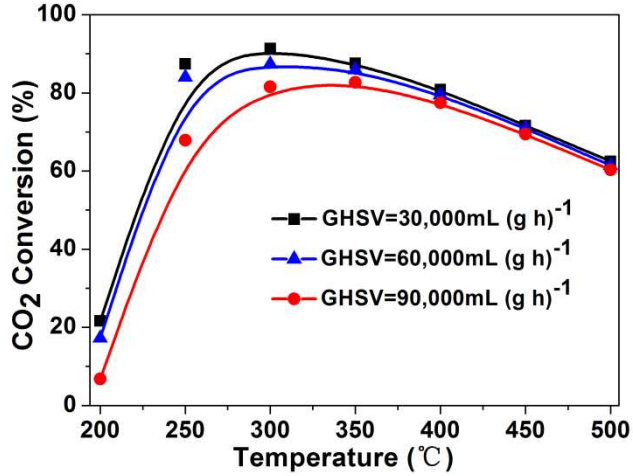

Fig. 11 The curves of the CO_2 conversion versus temperature at various gas hourly space velocities (GHSV) on $Ni_{0.8}Mg_{0.2}O$@SiO_2-R catalyst.

3.2.3 The effect of GHSV

The effect of GHSV on the catalytic performances of $Ni_{0.8}Mg_{0.2}O$@SiO_2-R catalyst reduced at 450 ◦C was investigated. The results of CO_2 methanation reaction expressed as the CO_2 conversion and CH_4 selectivity versus temperature were laid out in Fig. 11. As can be seen in Fig. 11, with the increase of GHSV from 30,000 mL (g h)$^{-1}$ to 90,000 mL (g h)$^{-1}$ at the studied temperature, the conversion of CO_2 suffered from decline. This might be caused by the insufficient contact time of the CO_2 and H_2 which couldn't make the reaction complete. It could be observed in the Fig. S3 ESI† that the catalysts showed high CH_4 selectivity (> 97%) even at higher GHSV. Thus, Low GHSV was beneficial for CO_2 metanation at low temperature.

3.3 Catalyst stability

The long-term stability was performed on the $Ni_{0.8}Mg_{0.2}O$@SiO_2-R as it showed the best performance of other samples over the 8 h methanation reaction. It might be prone to suffer from the sintering of the Ni active centers due to its relatively high Ni content. Therefore it is representative sample to judge whether the silica shell was helpful for keeping the stability of the catalyst. Before the long-term tests, $Ni_{0.8}Mg_{0.2}O$ catalyst and $Ni_{0.8}Mg_{0.2}O$@SiO_2 catalyst were reduced under a total gas flow of 60mL min^{-1} (N_2/H_2=2/1) at 500 ◦C for 2 h in situ. The results of CO_2 conversion and CH_4 selectivity were displayed in Fig. 12. It was observed that $Ni_{0.8}Mg_{0.2}O$-100h suffered slightly decreasing of CO_2 conversion after 100h reaction and the loss in initial CO_2 conversion was about 4%. Comparing to $Ni_{0.8}Mg_{0.2}O$-100h catalyst, $Ni_{0.8}Mg_{0.2}O$@SiO_2-100h catalyst exhibited high catalytic activity (87% for the conversion of CO_2, 99% for the selectivity of CH_4) and rather stable catalytic behavior during 100 h time on-stream under the same reaction conditions (Fig. 12).

The pattern of $Ni_{0.8}Mg_{0.2}O$@SiO_2-100h catalyst after 100 h reaction (Fig. 13A) showed very weak and broad peaks of Ni^0 (44.4 ° and 51.8 °), which was similar to that of $Ni_{0.8}Mg_{0.2}O$@SiO_2-R, indicating that Ni NPs still remained highly dispersion and no larger Ni NPs were formed (see TEM of $Ni_{0.8}Mg_{0.2}O$@SiO_2-100h (Fig. 13C). By comparison of the TEM images of $Ni_{0.8}Mg_{0.2}O$@SiO_2 before and after use, there was no obvious change. Fig. 13D showed high magnification TEM

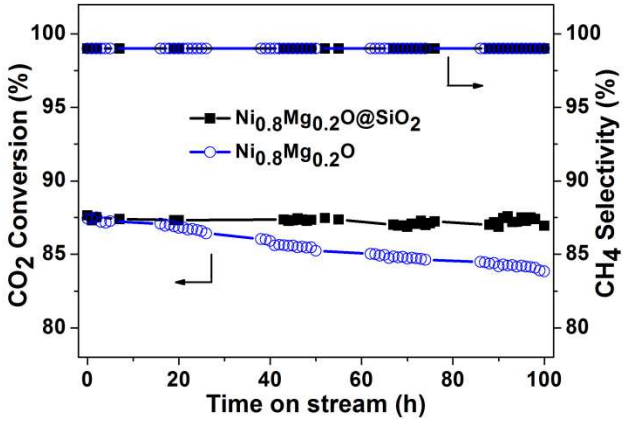

Fig. 12 Long-term stability tests of $Ni_{0.8}Mg_{0.2}$@SiO_2-R and $Ni_{0.8}Mg_{0.2}$O-R at 300 ◦C. Reaction condition: H_2/CO_2=4, GHSV=60,000 mL (g h)$^{-1}$, 1 atm

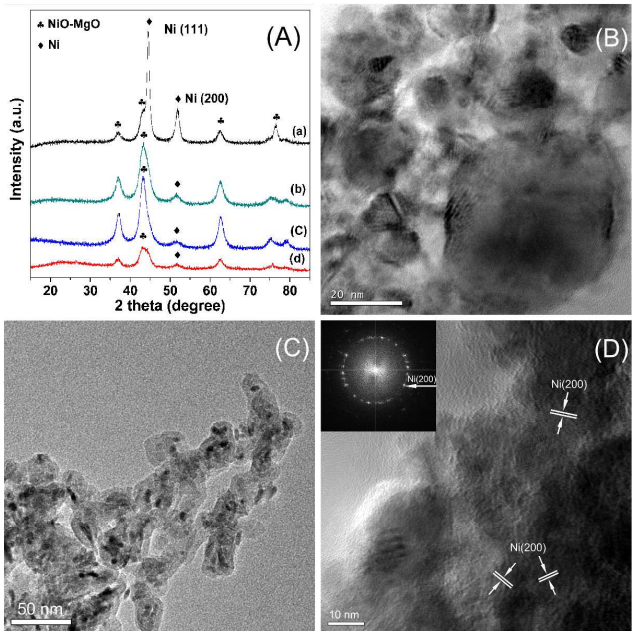

Fig. 13 (A) XRD patterns of (a): $Ni_{0.8}Mg_{0.2}$O-100h (b): $Ni_{0.8}Mg_{0.2}$O-R (c): $Ni_{0.8}Mg_{0.2}$O@SiO_2-R (d): $Ni_{0.8}Mg_{0.2}$O@SiO_2-100h; (B) High magnification TEM images of $Ni_{0.8}Mg_{0.2}$O-100h; Low(C) and high (D) magnification TEM images of $Ni_{0.8}Mg_{0.2}$O@SiO_2-100h and corresponding FFT (inset in panel D)

image of $Ni_{0.8}Mg_{0.2}$O@SiO_2-100h catalyst. It can be seen that Ni^0 (200) planes were dominated. TG-DSC analysis of $Ni_{0.8}Mg_{0.2}$O-100h after 100 h long-term stability at 300 ◦C was performed (in Fig.S4, ESI†). The TG curve of the $Ni_{0.8}Mg_{0.2}$O-100h catalyst indicated a weight gain due to the oxidation of Ni^0. And there was no deposition carbon on $Ni_{0.8}Mg_{0.2}$O-100h catalyst. In Fig. 13A, the pattern of $Ni_{0.8}Mg_{0.2}$O-100h showed that the intensity of metallic Ni diffraction peaks became stronger and sharper than $Ni_{0.8}Mg_{0.2}$O-R, suggesting that Ni NPs sintered to larger particles with time on stream without the protection of the silica shell. The Ni particle sizes of catalyst $Ni_{0.8}Mg_{0.2}$O-100h calculated by the Scherrer equation were 23.1 nm (111) and 11.9 nm (200). Based on the TEM images of $Ni_{0.8}Mg_{0.2}$O-100h catalyst after long-term test (Fig. 13B), the aggregation of $Ni_{0.8}Mg_{0.2}$O-100h catalyst was significant. Additionally, BET measurements revealed that the surface area of $Ni_{0.8}Mg_{0.2}$O-100h decreased from 144.89 to 36.05 m^2 g^{-1} after 100 h reaction at 300 ◦C. There was no major change in the surface area of $Ni_{0.8}Mg_{0.2}$O@SiO_2-100h before (134.27 m^2 g^{-1}) and after long-term test (113.43 m^2 g^{-1}). Therefore the significant decrease in surface area for the catalyst $Ni_{0.8}Mg_{0.2}$O-100h might be an additional reason for the observed deactivation. In other words, the confinement effect of the silica shell kept the 'size effect' of the Ni NPs during the reaction and promoted the catalytic stability.

Conclusions

Core-shell nano-catalysts Ni_xMg_yO@SiO_2 with various Ni/Mg ratios were facilely prepared by chemical co-precipitation process and modified Stöber method. The catalyst $Ni_{0.8}Mg_{0.2}$O@SiO_2-R was found to be highly active and selective for CO_2 methanation at low temperature. Long-term experiments performed for 100 h at 300 ◦C showed that no deactivation of the catalysts was observed. We believed that the highly dispersed Ni NPs formed during the reduction process of $Ni_{0.8}Mg_{0.2}O$ solid solution and isolated by silica shell contributed to the enhanced low-temperature activity and stability for CO_2 methanation.

Acknowledgment

This work is supported by the National Science Foundation of China (21173242), 973 Program and 863 Program of Department of Sciences and Technology of China (Grant Nos. 2007CB613305, 2009CB22003, and 2009AA05Z117).

References

1. T. R. Karl and K. E. Trenberth, *Science*, 2003, **302**, 1719-1723.
2. G. Fu, G. Lv and J. Ma, *J. Mol. Catal.(China)*, 2013,**27**, 218-226.
3. S. D. Kenarsari, D. Yang, G. Jiang, S. Zhang, J. Wang, A. G. Russell, Q. Wei and M. Fan, *RSC Adv.*, 2013, **3**, 22739-22773.
4. X. D. Xu and J. A. Moulijn, *Enery Fuels*, 1996, **10**, 305-325.
5. N. S. Siefert and S. Litster, *Appl. Energy*, 2013, **107**, 315-328.
6. M. Aresta and A. Dibenedetto, *Dalton Trans.*, 2007, **28**, 2975-2992.
7. H. Chen, Y. Liang, X. Zheng and X. Zhao, *J. Mol. Catal.(China)*, 2013, **27**, 556-l565.
8. T. Wu, W. Cai, P. Zhang, X. Song and L. Gao, *RSC Adv.*, 2013, **3**, 23976-23979.
9. Q. Ma, D. Wang, M. Wu, T. Zhao, Y. Yoneyama and N. Tsubaki, *Fuel*, 2013, **108**, 430-438.
10. W. Wang, S. Wang, X. Ma and J. Gong, *Chem. Soc. Rev.*, 2011, **40**, 3703-3727.
11. Y. Zhang, J. Deng, S. Zhang, K. Wang and J. Wu, *J. Mol. Catal. (China)*, 2013, **27**, 235-241.
12. S. N. Riduan and Y. Zhang, *Dalton Trans.*, 2010, **39**, 3347-3357.
13. Y. H. P. Zhang, *Int. J. Hydrogen Energy*, 2010, **35**, 10334-10342.
14. S. A. Park and H. Tak, *Ann. Reg. Sci.*, 2012, **49**, 261-287.
15. A. Beuls, C. Swalus, M. Jacquemin, G. Heyen, A. Karelovic and P. Ruiz, *Appl. Catal., B*, 2012, **113**, 2-10.
16. S. Sharma, Z. Hu, P. Zhang, E. W. McFarland and H. Metiu, *J. Catal.*, 2011, **278**, 297-309.
17. N. Srisawad, W. Chaitree, O. Mekasuwandumrong, A. Shotipruk, B. Jongsomjit and J. Panpranot, *Reac. Kinet. Mech. Catal.*, 2012, **107**, 179-188.
18. J. N. Park and E. W. McFarland, *J. Catal.*, 2009, **266**, 92-97.
19. W. Wei and G. Jinlong, *Front. Chem. Sci. Eng.*, 2011, **5**, 2-10.
20. M. D. E. Cai, J. Wen, W. Chu, X. Q. Cheng and Z. J. Li, *J. Nat. Gas Chem.*, 2011, **20**, 318-324.
21. T. Abe, M. Tanizawa, K. Watanabe and A. Taguchi, *Energy Environ. Sci.*, 2009, **2**, 315-321.
22. J. Liu, C. Li, F. Wang, S. He, H. Chen, Y. Zhao, M. Wei, D. G. Evans and X. Duan, *Catal. Sci. Technol.*, 2013, **3**, 2627-2633.
23. S. Tada, T. Shimizu, H. Kameyama, T. Haneda and R. Kikuchi, *Int. J. Hydrogen Energy*, 2012, **37**, 5527-5531.
24. G. A. Du, S. Lim, Y. H. Yang, C. Wang, L. Pfefferle and G. L. Haller, *J. Catal.*, 2007, **249**, 370-379.
25. Y. H. Hu, *Catal. Today*, 2009, **148**, 206-211.
26. J. A. S. P. Carreiro and M. Baerns, *J. Catal.*, 1989, **117**, 258-265.

27. T. Nakayama, N. Ichikuni, S. Sato and F. Nozaki, *Appl. Catal., A,* 1997, **158**, 185-199.
28. A. Parmaliana, F. Arena, F. Frusteri and N. Giordano, *J. Chem. Soc. Faraday Trans.*, 1990, **86**, 2663-2669.
29. A. Kuzmin and N. Mironova, *J. Phys. Condens. Matter.*, 1998, **10**, 7937-7944.
30. Y.-H. Wang, H.-M. Liu and B.-Q. Xu, *J. Mol. Catal. A: Chem.,* 2009, **299**, 44-52.
31. A. J. Forman, J.-N. Park, W. Tang, Y.-S. Hu, G. D. Stucky and E. W. McFarland, *ChemCatChem*, 2010, **2**, 1318-1324.
32. J.-N. Park, A. J. Forman, W. Tang, J. Cheng, Y.-S. Hu, H. Lin and E. W. McFarland, *Small*, 2008, **4**, 1694-1697.
33. J. C. Park, J. U. Bang, J. Lee, C. H. Ko and H. Song, *J. Mater. Chem.*, 2010, **20**, 1239-1246.
34. X. Shihong, S. Wenfeng, Y. Jian, C. Mingxia, S. Jianwei and J. Zhi, *Nanotechnology*, 2008, **19**, 095606.
35. L. Li, P. Lu, Y. Yao and W. Ji, *Catal. Commun.*, 2012, **26**, 72-77.
36. L. Li, S. He, Y. Song, J. Zhao, W. Ji and C.-T. Au, *J. Catal.*, 2012, **288**, 54-64.
37. Y. J. O. Asencios, J. D. A. Bellido and E. M. Assaf, *Appl. Catal., A*, 2011, **397**, 138-144.
38. M. Kong, Q. Yang, J. Fei and X. Zheng, *Int. J. Hydrogen Energy*, 2012, **37**, 13355-13364.
39. Q. S. Jing and X. M. Zheng, *Energy*, 2006, **31**, 2184-2192.
40. A. Torrisi, A. Cavallaro, A. Licciardello, A. Perniciaro and S. Pignataro, *Surf. Interface Anal.*, 1987, **10**, 306-310.
41. N. Takezawa, H. Terunuma, M. Shimokawabe and H. Kobayashib, *Appl. Catal.*, 1986, **23**, 291-298.
42. F. Arena, A. Licciardello and A. Parmaliana, *Catal. Lett.*, 1990, **6**, 139-149.
43. Y. H. Hu and E. Ruckenstein, *Catal. Lett.*, 1997, **43**, 71-77.
44. A. Zecchina, G. Spoto, S. Coluccia and E. Guglielminotti, *J. Chem. Soc. Faraday Trans. 1*, 1984, **80**, 1875-1889.

Graphical abstract